Review of Scientific Instruments

Measurement of L-shell emission from mid-Z targets under non-LTE conditions using Transmission Grating Spectrometer and DANTE power diagnostics

Cite as: Rev. Sci. Instrum. **92**, 033502 (2021); https://doi.org/10.1063/5.0040574
Submitted: 14 December 2020 . Accepted: 09 February 2021 . Published Online: 01 March 2021

M. Fraenkel, Y. Ehrlich, Z. Shpilman, Z. Henis, Y. Frank, E. V. Marley, G. Pérez-Callejo, J. Emig, R. F. Heeter, D. A. Liedahl, M. E. Foord, and M. B. Schneider

Review of Scientific Instruments ARTICLE scitation.org/journal/rsi

Measurement of L-shell emission from mid-Z targets under non-LTE conditions using Transmission Grating Spectrometer and DANTE power diagnostics

Cite as: Rev. Sci. Instrum. 92, 033502 (2021); doi: 10.1063/5.0040574
Submitted: 14 December 2020 • Accepted: 9 February 2021 •
Published Online: 1 March 2021

M. Fraenkel,[1,a)] Y. Ehrlich,[1] Z. Shpilman,[1] Z. Henis,[1] Y. Frank,[2] E. V. Marley,[2] G. Pérez-Callejo,[3,4] J. Emig,[2] R. F. Heeter,[2] D. A. Liedahl,[2] M. E. Foord,[2] and M. B. Schneider[2]

AFFILIATIONS

[1]Plasma Physics Department, Soreq NRC, Yavne 81800, Israel
[2]Lawrence Livermore National Laboratory, Livermore, California 94551, USA
[3]Clarendon Laboratory–University of Oxford, Parks Road, Oxford OX1 3PU, United Kingdom
[4]Université de Bordeaux-CNRS-CEA, Centre Lasers Intenses et Applications (CELIA), UMR 5107, F-33405 Talence, France

Note: This paper is published as part of the Special Topic on Proceedings of the 23rd Topical Conference on High-Temperature Plasma Diagnostics.
[a)]**Author to whom correspondence should be addressed:** moshe@soreq.gov.il

ABSTRACT

In this work, we present the measurement of L-band emission from buried Sc/V targets in experiments performed at the OMEGA laser facility. The goal of these experiments was to study non-local thermodynamic equilibrium plasmas and benchmark atomic physics codes. The L-band emission was measured simultaneously by the time resolved DANTE power diagnostic and the recently fielded time integrated Soreq-Transmission Grating Spectrometer (TGS) diagnostic. The TGS measurement was used to support the spectral reconstruction process needed for the unfolding of the DANTE data. The Soreq-TGS diagnostic allows for broadband spectral measurement in the 120 eV–2000 eV spectral band, covering L- and M-shell emission of mid- and high-Z elements, with spectral resolution $\lambda/\Delta\lambda$ = 8–30 and accuracy better than 25%. The Soreq-TGS diagnostic is compatible with ten-inch-manipulator platforms and can be used for a wide variety of high energy density physics, laboratory astrophysics, and inertial confinement fusion experiments.

I. INTRODUCTION

In many high energy density physics (HEDP) Inertial Confinement Fusion (ICF) programs[1,2] and laboratory astrophysics experiments[3,4] performed at laser and pulsed power facilities, the measurement of soft x rays emitted from the target is needed for diagnosing the plasma conditions and studying the relevant physics under consideration. In most HEDP facilities, the broadband x-ray emission is measured by using an array of x-ray diodes, such as the DANTE power diagnostic, which is operational at the OMEGA laser,[5] the National Ignition Facility (NIF),[6] and similar devices at other laser facilities worldwide.[7] This tool, designed primarily to measure near Local Thermodynamic Equilibrium (LTE) hohlraum emission, provides an absolutely calibrated measurement of the time-resolved x-ray emission at discrete spectral bands, and the "complete" spectral shape can be obtained through a spectral unfolding and reconstruction process. The spectral unfolding process is usually based on assumptions regarding the emitted spectrum of the source, such as near Local Thermodynamic Equilibrium (LTE) or Planckian spectrum. In applications where these assumptions cannot be justified, the accuracy of the spectral unfolding process and the reconstructed spectrum is obviously limited.[8]

Another widely used x-ray diagnostics is the Transmission Grating Spectrometer (TGS),[9–11] a relatively simple apparatus that

consists of only a transmission grating and a detector. The x-ray radiation, emitted from the target, is dispersed by the grating according to Bragg's law,

$$\sin(\theta) = m\frac{\lambda}{d}, \quad (1)$$

where λ is the wavelength, d is the grating period, and m is the order of diffraction. A detector, either time resolved or time integrated, is positioned at some distance from the grating. When a 2D detector is used [e.g., CCD camera, Image Plate (IP), or framing camera], the pin-hole nature of the grating allows us to spatially resolve the source along the axis perpendicular to the dispersion axis. The device's spectral bandwidth and spectral resolution depend on the wavelength, grating's parameters, grating to detector distance, source size, and the detector's spatial resolution. The resolution is limited by the number of periods of the grating, $\lambda/\Delta\lambda \le N$, typically on the order of a few tens, and by the geometrical projection of the source size on the detector. Traditional TGS is known to cause overlapping of high dispersion orders, thus limiting the accuracy of the wide spectral band measurement. Recently,[12] a sinusoidal transmission grating (STG) was demonstrated, which efficiently diminishes high diffraction orders, allowing higher accuracy measurements.

In recent years, an effort is underway to develop an experimental platform at the OMEGA laser to study non-LTE (NLTE) plasmas of various materials.[13–15] In this buried layer approach, a 250 μm–350 μm diameter, 2000 Å thick dot of mid-Z target material is placed at the center of 1000 μm diameter, 10 μm thick beryllium tamper. Laser beams heat the target from both sides for several ns. Side-on and face-on x-ray imagers are used to measure the size of the emitting volume vs time from which the density is inferred. The electron temperature is measured using the K-shell spectral lines ratio. The L-shell spectrum is measured using x-ray spectrometers to benchmark NLTE atomic codes.

In order to enhance the diagnostic suite for the buried-layer experiments and specifically to have better support for the NLTE broadband spectral measurement, a Ten-Inch-Manipulator (TIM)-based TGS has been fielded at the OMEGA laser facility and was recently tested at shots with Ti buried layer targets.[15] The Soreq-TGS was partially calibrated and provides another broadband spectral measurement in addition to the DANTE. Unlike the DANTE, the Soreq-TGS is not limited by any source assumptions and has a higher spectral resolution over a large bandwidth: $\lambda/\Delta\lambda$ of 8–30 throughout the relevant spectral range of 120 eV–2000 eV, which covers L- and M-shell emission of mid Z materials. As recently demonstrated,[8,12] a combined measurement by an x-ray diode array such as the DANTE, and a TGS diagnostics, can provide a high-accuracy, broadband, and time resolved spectral measurement. In this paper, we demonstrate the use of these two diagnostics for combined measurements of L-band emission from Sc/V buried layer targets at the OMEGA laser facility and compare the results to 1D and 2D radiation hydrodynamic simulations.

In Sec. II, the TGS system is described, the design considerations are explained, and the partial calibration process is detailed. In Sec. III, results of recent buried layer experiments at the OMEGA laser are presented and discussed. These include L-shell Sc/V emission spectral measurements, which were acquired using the DANTE and the TGS diagnostics simultaneously. The results show good agreement with simulations performed using 1D and 2D radiation hydrodynamic codes, where both use tabulated NLTE opacities calculated using the atomic code SEMILLAC.[16] Section IV summarizes this work.

II. SOREQ-TGS DIAGNOSTIC

A. General description and accuracy

In its most basic version, a TGS is composed of the transmission grating and an x-ray sensitive detector. The grating is made by "writing" a periodic transmission function onto a substrate of high-Z material (usually gold), which efficiently absorbs soft x rays. According to Bragg's law (1), for a typical d = 1 μm period grating, the first order dispersion of λ = 10 nm wavelength radiation will be deflected by an angle of $\alpha = 0.6^\circ$. The deflection angle is a primary parameter for the design of the grating-to-source distance, which for a given detector determines the spectral bandwidth and resolution. A basic grating is made of free standing high-Z bars and has a square binary transmission function. Such a grating is known to produce high diffraction orders and, for a wide bandwidth spectrum, causes overlapping of different orders at the same location on the detector, thus limiting the measurement accuracy. In this work we have used a sinusoidal transmission grating (STG),[12] which efficiently diminishes higher diffraction orders, allowing a highly accurate measurement. The grating's fabrication technique was described elsewhere.[10] As will be shown in Sec. II B, the grating's transmission function, which is needed for the diagnostic's calibration, was measured with an accuracy better than ±10%. The detector was a back-illuminated time-integrated x-ray CCD (XRCCD) camera. We have used a Spectral Instruments 800 series x-ray CCD (XRCCD) camera housed in an OMEGA TIM. The camera sensitivity was not directly measured, and therefore, quantum efficiency measurements of similar CCD detectors[17] and manufacturer data of amplifier's gain for the specific camera were used to transform from the gray level image to physical unit data (see Fig. 1). Based on the experience with similar detectors, we can assume an accuracy of ±20% on the detector sensitivity when using gain data. Additional uncertainties may originate from impurities evaporated on the detector throughout its usage, which usually affect only the soft part of the spectral range and are not expected to degrade the CCD sensitivity by more than 10%.[18] The other uncertainties (mostly geometric) in the system are much smaller. The uncertainties in the grating and detector response functions are added in quadrature to obtain the Soreq-TGS

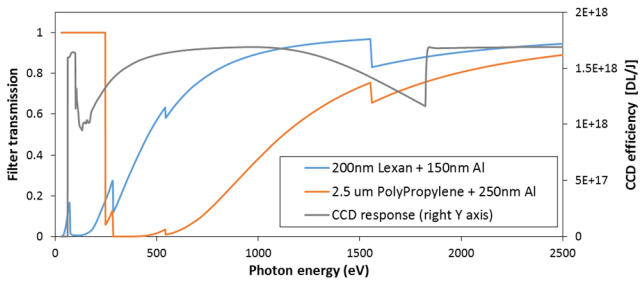

FIG. 1. CCD response function used for conversion from digital levels to physical units. Also included are the calculated[22] transmission functions of the filters used, as explained in Sec. III.

soft x-ray measurement accuracy. The accuracy is found to be better than 25%, which is acceptable for most spectroscopic and atomic physics applications. In Sec. III, the Soreq-TGS measurement will be compared against the DANTE results, and good agreement between absolute measurements will support the TGS calibration accuracy.

B. Grating's transmission function calibration

The grating's transmission function is determined by the exact substrate material composition and the relative area of the opened structures. The transmission is a superposition of the radiation, which goes through the openings, and the energy-dependent transmission through the substrate. The traditional transmission grating efficiency was summarized by Eidmann *et al.*[19] based on the Fraunhofer theory of diffraction.[20] A sinusoidal grating has only three diffraction orders: zero order and both positive and negative first orders.[21] A detailed simulation code based on the Huygens–Fresnel principle[12] shows that the transmission efficiency η_m for the mth diffraction order is

$$\eta_0 = a^2\left(1 + T + 2\varphi\sqrt{T}\right),$$
$$\eta_1 = \left(\frac{a^2}{4}\right)\left(1 + T - 2\varphi\sqrt{T}\right), \quad (2)$$
$$\eta_{m>1} = 0,$$

where T is the transmission through the grating substrate, a is the relative area occupied by the openings ($a = 1/2$ for a perfect symmetric sinusoidal grating), and $\varphi = \cos\left((2\pi\sum_i(n_{1i}-1)z_i)/\lambda\right)$ represents the interference of the radiation, which goes through the openings with the radiation transmitted through the substrate. The substrate is composed of several layers with thickness z_i and the real part of refraction index n_{1i}. We implement the sinusoidal grating as a series of openings in the substrate, each with sinusoidal shape whose contours follows $\pm A(1 + \sin(2\pi kx))$ lines, as shown in Fig. 2. The grating period $d = 1/k$ should be determined by the experimental requirements (spectral resolution and detector size), and A determines the opening's height and therefore the grating's transmission efficiency. In our grating, the substrate is made of a 200 nm thick Si_3N_4 base layer, a 10 nm Ti adhesion layer, and the main 400 nm thick Au layer. The grating's efficiency model, calculated using refraction index data from the Henke database[22] and structure-dependent factor from the Scanning Electron Microscope (SEM) image, should be benchmarked against calibration experiments to reduce uncertainties in all inputs, the most important of which are the manufacturing tolerances of the layers thicknesses.

TABLE I. Filter combinations, targets, and laser intensities used to create the narrow band spectral windows for the grating calibration. The photon energy column specified the spectral band›s weighted center.

Photon energy (eV)	Filter combination (thicknesses in μm)	Target	Laser intensity (W/cm^2)
250	Lexan 2	Ti	5×10^{12}
400	Ti 0.4	Ti	1×10^{13}
1200	Mg 5	Cu	2×10^{14}
1320	Al 5 + Ti 0.4	Au	2×10^{14}
1390	Si 8	Au	2×10^{14}
2500	Mylar 25 + Mo 1	Au	2×10^{14}

The calibration experiments have been performed at the Soreq plasma physics laboratory. The grating was positioned alongside a pinhole of known diameter at an equal distance to a gold disk target. A 1 ns duration laser pulse of 5 J–10 J was focused onto the target to intensities up to 2×10^{14} W/cm^2 and created a broadband x-ray source for the calibration. Several targets, filter combinations, and laser intensities were chosen to select narrow band spectral windows, as listed in Table I. The source radiation that passed through the filters was either dispersed by the grating or passed through the pinhole, thus forming two signals on the same CCD detector. The ratio of the first order diffraction signal to the pin-hole signal (normalized to the pinhole's area) is the grating transmission efficiency

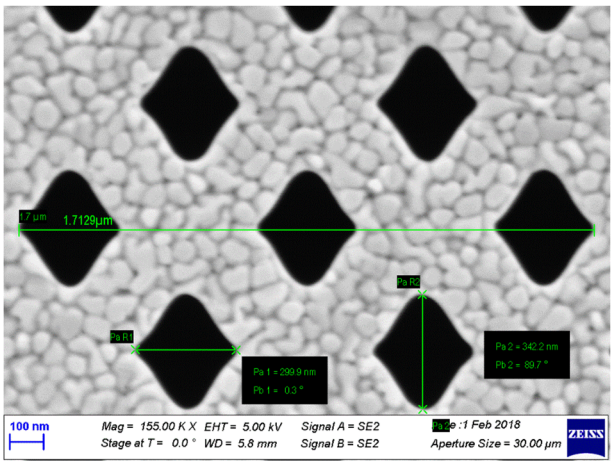

FIG. 2. Scanning Electron Microscope (SEM) image showing part of the sinusoidal transmission grating. The diffraction direction is horizontal. Additional periodic structures on directions other than the horizontal cause more diffraction patterns on the detector, but these usually do not disturb the main diffraction pattern.

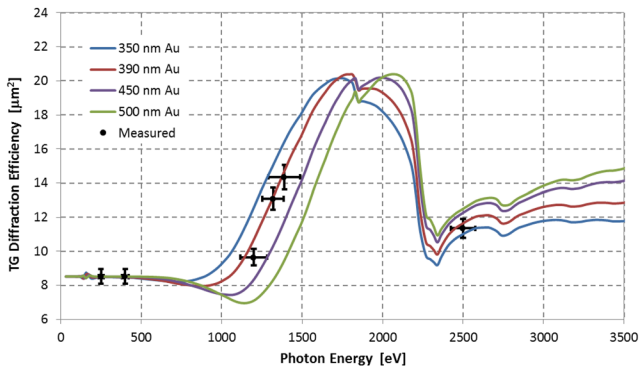

FIG. 3. Measured transmission into the first order of diffraction of the TG used in the experiments. Shown are data points with error bars. The transmission model with a gold layer thickness of 390 nm best fits the data. Models with other thicknesses are shown for comparison.

TABLE II. Grating parameters and working distances for the Soreq-TGS diagnostics and the resulting spectral coverage and resolution.

Grating period	367 nm
Spectral coverage	150 eV–2000 eV
Grating size	31 × 23 $(\mu m)^2$
Grating efficiency (effective cross section)	8.5 $(\mu m)^2$ @ 200 eV 13 $(\mu m)^2$ @ 1300 eV
Source to grating distance	1770 mm
Grating to detector distance	740 mm
Magnification	0.4
Distance on detector from zero-order to 2000 eV emission	1.2 mm
Spectral resolution (limited by source size projection on the detector, inc. diffraction)	λ/Δλ = 13 @ 1300 eV λ/Δλ = 8.4 @ 2000 eV
Spatial resolution	400 μm @ 250 eV 120 μm @ 1000 eV

for the specific energy band in terms of effective area. The grating's calibration results are shown in Fig. 3. The accuracy is ±3%–7% in the horizontal axis, mainly due to the finite spectral bands of the filter combination, and ±5% in the vertical axis, mainly due to signal-to-noise ratio and pin-hole size uncertainty. Thicknesses of the grating's substrate layers were used as free parameters of the model, most sensitive of which was the gold layer's thickness. As shown in Fig. 3, the model with 390 nm thick gold layer best matches the data and was chosen as the grating's efficiency function. The other plots with different gold layer thicknesses are shown for comparison. The overall grating calibration accuracy is estimated to be better than ±10%.

C. Soreq-TGS design and evaluation experiment

The grating's parameters and working distances that were chosen for the Soreq-TGS design are presented in Table II. Also shown in the table are the expected spectral coverage on the CCD detector and spectral resolution. The grating and working distances were chosen so that the expected emission intensity, as calculated by a radiation-hydrodynamic code,[15] will be well inside the detector's dynamic range. It should be emphasized that the grating can easily be changed between campaigns, so other requirements can be met if needed.

The Soreq-TGS was fielded for a Ti buried layer target campaign at OMEGA and performed as expected. A Ti spectrum acquired during the evaluation experiments and the comparison to radiation-hydrodynamic simulation were recently published.[15]

III. MEASUREMNTS OF BURIED LAYER TARGET EMISSION USING DANTE AND TGS DIAGNOSTICS

Buried layer experiments with Sc/V targets were performed at OMEGA in which both DANTE and Soreq-TGS diagnostics were positioned at relatively close polar angles to the target: DANTE at 60° and TGS at 44° to target normal. The buried layer target contained a Sc/V dot (2000 Å thick and 250 μm or 350 μm in diameter) inside a Be tamper. Each target had a Ti timing fiducial target attached to the target stalk (see Fig. 4 for target design). The TGS had a viewing angle of 35° to the target stalk. In order to spatially resolve the different targets, the TGS was rotated so that the dispersion axis was almost perpendicular, and the spatial resolution axis was almost parallel to the stalk. 18 OMEGA laser beams illuminated the target from each side for 3 ns at an intensity of 3.5×10^{14} W/cm^2. Two additional beams heated the fiducial target 5 ns after the main beams.

Raw data of DANTE measurement of shot 94 846 are presented in Fig. 5. The buried target emission can be seen in the first 3 ns–4 ns alongside the laser temporal pulse shape, whereas the fiducial target emission follows and is used to synchronize the voltage signals. Each waveform represents a different spectral channel centered at energies that are listed in the legend. The low energy emission recorded by the first two channels is the thermal emission from the Be tamper, which rises immediately, while the Sc/V emission is delayed by the time it takes for the heat front to reach the buried layer.

Also shown in Fig. 5 is a raw data image of the TGS measurement for the same shot as acquired by the CCD detector. The main dispersion line is marked by the red dashed line. All other dispersion lines are the result of secondary periodic structures in the grating and should be disregarded (see the explanation in the caption of Fig. 2). The zero order was blocked, and the higher energy part of the spectrum was filtered by thin (metalized polypropylene) light-tight foil to attenuate visible light diffracted by the grating. Due to low SNR, data for the 200 eV–500 eV region were taken from shot 94 842 (identical to 94 846) using thinner (metalized Lexan) light-blocking filter. The

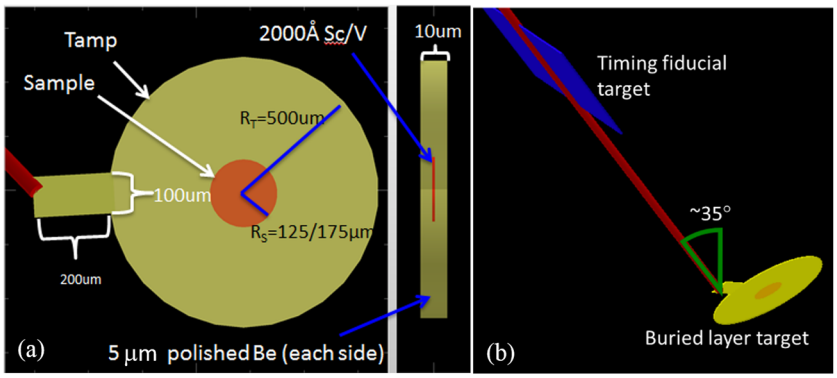

FIG. 4. (a) Face-on and side-on buried layer target design. (b) Soreq-TGS view of the target showing both the buried layer and the fiducial targets.

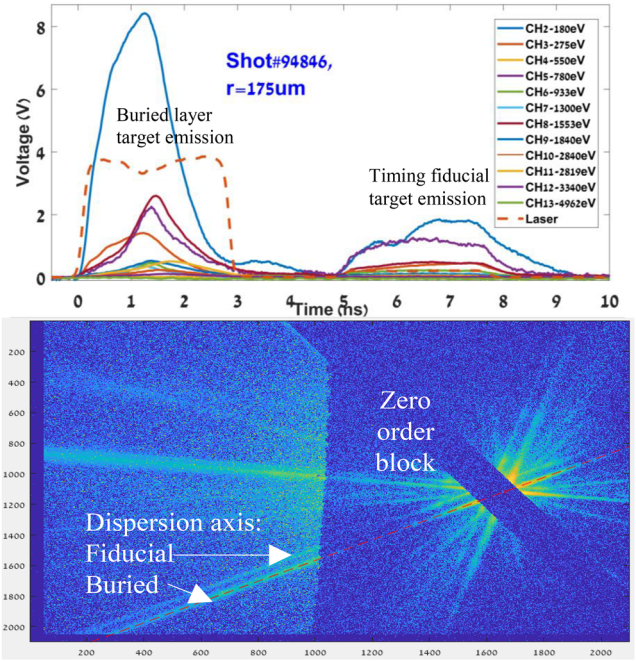

FIG. 5. Raw data of DANTE (top) and TGS (bottom) measurement of the Sc/V buried layer experiment at OMEGA. Both results are then combined to create a temporal/spectral map of the target emission.

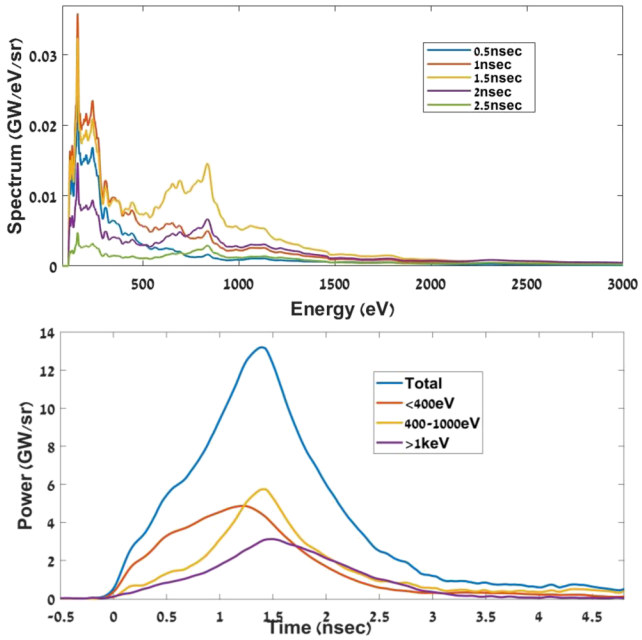

FIG. 7. Spectrum at several time points (top) and power at several spectral bands (bottom) inferred from the temporal/spectral map created by unfolding the DANTE results using the TGS time integrated spectrum. The emission at energies below 400 eV is mainly contributed by the Be tamper layer, while the higher energies are the Sc/V L-band emission.

filter compositions and calculated transmission functions are presented in Fig. 1. The double dispersion line structure is due to the spatial separation of the buried layer and fiducial target, which are resolved thanks to the pin-hole nature of the grating. The spatial resolution (specified in Table I) is sufficient to differentiate between the contributions of each target but is not intended to spatially resolve the buried target emission itself.

In Fig. 6, the time integrated buried layer emission spectrum is shown, as inferred from the TGS image in Fig. 5. The intensities are corrected to the grating's and detector's response functions, filter transmission, and working distances. The spectrum shows the

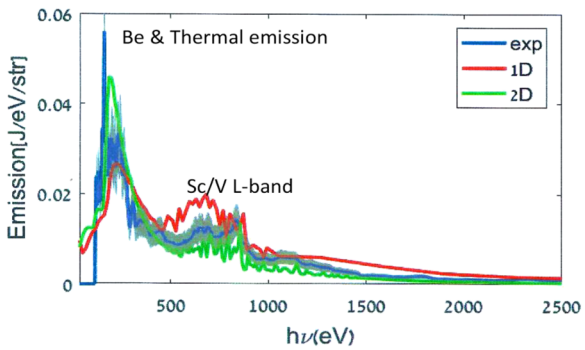

FIG. 6. Time integrated Sc/V buried layer target emission inferred from the TGS raw data shown in Fig. 5 (blue, accompanied with data uncertainties). Also shown are the results of 1D (red) and 2D (green) simulations.

Sc/V L-shell transitions at 400 eV–1500 eV as well as lower energy Be emission. As discussed above, the uncertainty in the spectrum intensity is 25%. Also shown in the figure are 1D and 2D simulations of the target emission, both in good agreement with the data. Comparison of the TGS data to the calibrated DANTE measurements shows agreement of better than 20% over most of the spectral band, with differences of up to 30% for few low-energy DANTE channels, which can be explained by the DANTE[5] and TGS (see Sec. II A) calibration accuracy.

As mentioned above, once DANTE voltage signals are acquired, spectral unfolding and reconstruction process is needed to provide the complete time resolved spectral shape. Here, we apply the previously proposed[8,12] method of DANTE spectral unfolding using the TGS time integrated result. The basic principle of this method is that the spectrum temporal evolution is derived from the DANTE channel results, while the more detailed spectral features are taken from the time integrated TGS measurement. A reconstructed temporal/spectral map is calculated, from which lineouts such as spectra at different time points or power at specific spectral bands can be inferred, the examples of which are shown in Fig. 7. Thanks to the rich spectral data acquired by the TGS, the spectra at various time points have much more detailed information than available when using just the DANTE results.

IV. CONCLUSION

The measurement of L-band emission from buried Sc/V targets in experiments at the OMEGA laser facility has been shown. The

goal of these experiments was to study NLTE plasmas and benchmark atomic physics codes. The L-band emission was measured simultaneously by the time resolved DANTE power diagnostic and the time integrated Soreq-TGS diagnostic. The TGS measurement provided an additional quantitative spectral measurement and was used during the spectral reconstruction process needed for unfolding the DANTE data. The Soreq-TGS diagnostic allows for the measurement of spectra in the 120 eV–2000 eV spectral band, covering L- and M-shell emission of mid- and high-Z elements. The measurement accuracy is better than 25% and can be further improved by a CCD detector calibration effort. Extension of the previous IP calibration work[23] is also possible, thus allowing for the use of IP for the absolutely calibrated spectrum measurement.

Although the Soreq-TGS was designed primarily for the non-LTE buried layer campaigns, due to its simple design and broadband coverage, it can be used for other applications with minor or no adaptations. With the proper choice of grating and working distance, a wide range of spectroscopic measurements can be supported. Time resolved measurements are also possible by adapting to the proper detector.

ACKNOWLEDGMENTS

The authors acknowledge the support of the technical staff at Soreq NRC and LLE and of the Soreq TG fabrication team. Lawrence Livermore National Laboratory is operated by Lawrence Livermore National Security, LLC, for the U.S. Department of Energy, National Nuclear Security Administration, under Contract No. DE-AC52-07NA27344 (Report No. LLNL-CONF-817385).

DATA AVAILABILITY

The data that support the findings of this study are available from the corresponding author upon reasonable request.

REFERENCES

[1] J. D. Lindl, P. Amendt, R. L. Berger, S. G. Glendinning, S. H. Glenzer, S. W. Haan, R. L. Kauffman, O. L. Landen, and L. J. Suter, Phys. Plasmas **11**, 339 (2004).
[2] O. A. Hurricane *et al.*, Phys. Plasmas **21**, 056314 (2014).
[3] B. A. Remington, D. Arnett, R. P. Drake, and H. Takabe, Science **284**, 1488 (1999).
[4] N. L. Kugland *et al.*, Phys. Plasmas **20**, 056313 (2013).
[5] K. M. Campbell, F. A. Weber, E. L. Dewald, S. H. Glenzer, O. L. Landen, R. E. Turner, and P. A. Waide, Rev. Sci. Instrum. **75**, 3768 (2004).
[6] E. L. Dewald *et al.*, Rev. Sci. Instrum. **75**, 3759 (2004).
[7] See for example, J. L. Bourgade *et al.*, Rev. Sci. Instrum. **72**, 1173 (2001); S. Jiang *et al.*, Nucl. Fusion **59**, 032006 (2019).
[8] Y. Ehrlich, S. Cohen, Y. Frank, A. Malka, G. Hurvitz, I. Levy, J. Davis, P. A. Keiter, R. P. Drake, D. Shvarts, M. Fraenkel, and Z. Shpilman, Rev. Sci. Instrum. **88**, 043507 (2017).
[9] M. Born and E. Wolf, *Principles of Optics*, 7th ed. (Cambridge University Press, 2003), pp. 446–461.
[10] N. M. Ceglio, R. L. Kauffman, A. M. Hawryluk, and H. Medecki, Appl. Opt. **22**, 318 (1983).
[11] G. Hurvitz, Y. Ehrlich, G. Strum, Z. Shpilman, I. Levy, and M. Fraenkel, Rev. Sci. Instrum. **83**, 083109 (2012).
[12] Z. Shpilman, G. Hurvitz, L. Danon, T. Shussman, Y. Ehrlich, S. Maman, I. Levy, and M. Fraenkel, Rev. Sci. Instrum. **90**, 013501 (2019).
[13] E. V. Marley *et al.*, Rev. Sci. Instrum. **89**, 10F106 (2018).
[14] G. Pérez-Callejo *et al.*, Phys. Plasmas **26**, 063302 (2019).
[15] Y. Frank, G. E. Kemp, E. V. Marley, G. P. Callejo, M. E. Foord, M. B. Schneider, Y. Ehrlich, and M. Fraenkel, Phys. Plasmas **27**, 063301 (2020).
[16] Y. Frank, P. Mandelbaum, and Z. Henis, High Energy Density Phys. **12**, 27 (2014).
[17] See for example, I. Moody, M. Watkins, R. Bell, M. Soman, J. Keelan, and A. Holland, CCD QE in the Soft X-ray Range, e2v Technologies technical report, https://www.teledyne-e2v.com/content/uploads/2017/03/SXRQE_white_paper_2017_Mar14.pdf, 2017.
[18] C. Reverdin *et al.*, Rev. Sci. Instrum. **75**, 3730 (2004).
[19] K. Eidmann, M. Kühne, P. Müller, and G. D. Tsakiris, J. X-Ray Sci. Technol. **2**, 259 (1990).
[20] See Ref. 5, p. 425.
[21] J. Kauppinen and J. Partanen, *Fourier Transform in Spectroscopy* (Wiley-VCH, Berlin, 2001), Sec. 9.5.
[22] B. L. Henke, E. M. Gullikson, and J. C. Davis, At. Data Nucl. Data Tables **54**, 181 (1993), available at http://henke.lbl.gov/optical_constants/.
[23] M. J. Haugh, J. Lee, E. Romano, and M. Schneider, "Calibrating image plate sensitivity in the 700 to 5000 eV spectral energy range," Proc. SPIE **8850**, 885007 (2013).